Systematics of isovector and isoscalar giant quadrupole resonances in normal and superfluid spherical nuclei

Guillaume Scamps[1,*] and Denis Lacroix[1,2,†]

[1]*GANIL, CEA/DSM and CNRS/IN2P3, Boîte Postale 55027, 14076 Caen Cedex, France*
[2]*Institut de Physique Nucléaire, IN2P3-CNRS, Université Paris-Sud, F-91406 Orsay Cedex, France*

The isoscalar (IS) and isovector (IV) quadrupole responses of nuclei are systematically investigated using the time-dependent Skyrme energy density functional including pairing in the BCS approximation. Using two different Skyrme functionals, Sly4 and SkM*, respectively 263 and 324 nuclei have been found to be spherical along the nuclear charts. The time-dependent evolution of these nuclei has been systematically investigated, giving access to their quadrupole responses. It is shown that the mean energy of the collective high-energy state globally reproduces the experimental IS and IV collective energy but fails to reproduce their lifetimes. It is found that the mean collective energy depends rather significantly on the functional used in the mean-field channel. Pairing by competing with parity effects can slightly affect the collective response around magic numbers and induces a reduction of the collective energy compared to the average trend. Low-lying states, that can only be considered if pairing is included, are investigated. While the approach provides a fair estimate of the low-lying state energy, it strongly underestimates the transition rate $B(E2)$. Finally, the possibility to access the density dependence of the symmetry energy through parallel measurements of both the IS and IV giant quadrupole resonances is discussed.

I. INTRODUCTION

In recent years, large efforts have been devoted within the energy density functional (EDF) to bring time-dependent theories to the level of state-of-the-art nuclear structure theories. A current topic of interest is to include pairing correlations in nuclear dynamics [1–6]. In the present work, we systematically investigated the possibility to describe the isoscalar (IS) and isovector (IV) giant quadrupole resonances (GQRs) including pairing using the time-dependent Hartree-Fock + BCS (TDHF + BCS) approach. There are several reasons to have chosen the GQR as a test ground: (i) As far as we know, the isoscalar and isovector GQRs have never been systematically investigated using a time-dependent EDF framework, and therefore our study should make it possible to identify weakness and strength of this approach in this context. (ii) A systematic analysis exists using the quasiparticle random-phase approximataion (QRPA) approach allowing for comparisons [7]. (iii) A large amount of experimental data exists especially for the IS GQR [8–15] and therefore not only qualitative but also quantitative studies can be made. (iv) The experimental observation of the IV GQR has recently made some progress [16–18]. (v) Thanks to such progress, the GQR was recently proposed as a possible alternative tool to get information on the density dependence of the symmetry energy [19].

In the present work, we have systematically investigated the evolution of nuclei that are found spherical in their ground states using two different Skyrme functionals. The static properties and the dynamical evolution have been obtained consistently using the HF + BCS and TDHF + BCS

approaches. The TDHF + BCS method, while less general than the time-dependent Hartree-Fock-Bogoliubov (TDHFB) framework and leading to specific difficulties [5], has the advantage that each evolution can be simulated in a reasonable numerical time, allowing us to perform the calculation over a wide range of nuclei.

In the following, the microscopic approach is briefly described. Then, the protocol for selecting nuclei is discussed as well as some average properties related to the pairing correlations, the root-mean-square radius, etc. Properties of the response in the low-lying and high-lying sectors are investigated. We finally illustrate the usefulness of large scale GQR study with the possibility to infer from it information on the symmetry energy.

II. THE TDHF + BCS APPROACH TO GIANT RESONANCES

The TDHF + BCS theory is a simplified version of the TDHFB approach where the off-diagonal part of the pairing field is neglected. Properties, advantages, and drawback of this theory have been discussed extensively in Refs. [4–6] and we only give below a minimal summary of important aspects to treat giant resonances.

For a given nucleus, the initial wave function is obtained using the EV8 code [20] that solves the HF + BCS equations in r-space with the Skyrme functional in the mean-field term and with a contact interaction in the pairing channel. After this step, the N-body wave packet takes the form of a quasiparticle vacuum written in a BCS form as

$$|\Psi_0\rangle = \prod_{k>0} (u_k^0 + v_k^0 a_k^\dagger a_{\bar{k}}^\dagger)|-\rangle, \tag{1}$$

*scamps@ganil.fr
†lacroix@ganil.fr

where u_k^0 and v_k^0 are usual components of the quasiparticle states while $a_k^\dagger$ and $a_{\bar{k}}^\dagger$ are the creation operators of time-reversed single-particle states, denoted respectively by $|\varphi_k\rangle$ and $|\varphi_{\bar{k}}\rangle$.

It can be shown [4] that the state (1) is a stationary solution of the TDHF + BCS set of coupled equations given by

$$i\hbar\partial_t|\varphi_k\rangle = (h[\rho](t) - \eta_k(t))|\varphi_k\rangle,$$
$$i\hbar\dot{n}_k(t) = \kappa_k(t)\Delta_k^*(t) - \kappa_k^*(t)\Delta_k(t), \quad (2)$$
$$i\hbar\dot{\kappa}_k(t) = \kappa_k(t)(\eta_k(t) + \eta_{\bar{k}}(t)) + \Delta_k(t)(2n_k(t) - 1),$$

where $\eta_k(t) = \langle\varphi_k(t)|h[\rho]|\varphi_k(t)\rangle$ and where $n_k(t) = |v_k(t)|^2$ and $\kappa_k(t) = u_k^*(t)v_k(t)$ are respectively the occupation numbers and anomalous density components.

To study giant resonances, we follow the method standardly used in time-dependent approaches (see for instance [21]) and apply a small initial boost to the wave packet $|\Psi_0\rangle$:

$$|\Psi(t = 0)\rangle = e^{-i\lambda\hat{Q}}|\Psi_0\rangle, \quad (3)$$

where λ is a number that is small enough to ensure the validity of the linear approximation. $\hat{Q}$ here is an operator that depends on the type of modes one would like to study. In the present work, we are interested in the giant quadrupole response in spherical nuclei where the excitation operators are given by [7]

$$\hat{Q}_{20}^{IS} = e\sum_{i=1}^{A} r_i^2 Y_{20}(\Omega_i), \quad (4)$$

$$\hat{Q}_{20}^{IV} = \frac{eN}{A}\sum_{i=1}^{Z} r_i^2 Y_{20}(\Omega_i) - \frac{eZ}{A}\sum_{i=1}^{N} r_i^2 Y_{20}(\Omega_i), \quad (5)$$

respectively in the isoscalar and isovector channels and where A, N, and Z are respectively the total, neutron and proton numbers.

The boost (3) induces a local boost to the single-particle components while leaving the initial (u_k, v_k) components unchanged, i.e. $u_k(t_0) = u_k^0$ and $v_k(t_0) = v_k^0$. The response of the nucleus to the initial perturbation is studied by solving the coupled set of TDHF + BCS equations in time. The strength function can then be obtained by performing the Fourier transform of the evolution of the operator $\hat{Q}$. More precisely, we have [4,21]

$$S_Q(\omega) = \lim_{\lambda\to 0} -\frac{1}{\pi\lambda\hbar}\int_{t_0}^{\infty} dt\,[Q(t) - Q(t_0)]\sin(\omega t), \quad (6)$$

where

$$Q(t) \equiv \langle\Psi(t)|\hat{Q}|\Psi(t)\rangle = \sum_k \langle\varphi_k(t)|\hat{Q}|\varphi_k(t)\rangle n_k(t). \quad (7)$$

Note that here only spherical nuclei are considered and $Q(t_0) = 0$.

In practice, the time evolution cannot be performed up to infinite time and a damping factor is assumed, i.e., $\sin(\omega t) \to e^{-\Gamma_0 t/2\hbar}\sin(\omega t)$ in formula (6). Then, decomposing the small amplitude vibration on the eigenstates of the system, denoted by $|\Psi_\nu\rangle$, associated with energy $\hbar\omega_\nu = E_\nu - E_0$, E_0 being the

ground state energy, the strength function is

$$S_Q(E) = \frac{1}{2\pi}\sum_\nu |\langle\Psi_0|\hat{Q}|\Psi_\nu\rangle|^2$$
$$\times \left\{\frac{\Gamma_0}{(E - \hbar\omega_\nu)^2 + \Gamma_0^2/4} - \frac{\Gamma_0}{(E + \hbar\omega_\nu)^2 + \Gamma_0^2/4}\right\}. \quad (8)$$

In the zero-damping limit, one recovers the standard form of the strength function generally used in the RPA or QRPA [22]. Note that in the following, we will simply use the notation S_{IS} and S_{IV} for the isoscalar and isovector strength functions respectively.

A. Selection of nuclei

In the present study, we have systematically considered initial nuclei that are found to be spherical in the EV8 code. The mesh size has been taken as $\Delta x = \Delta y = \Delta z = 0.8$ fm and the total size of the mesh is $2L_x = 2L_y = 2L_z = 22.4$ fm. We have checked that the mesh is large enough to not bias the nuclear response in the considered nuclei. Two different functionals, namely the Sly4 [23] and the SkM* [24], have been employed in the mean-field channel. These two functionals have the advantage of being widely used in nuclei, allowing for comparison of the present results with other approaches such as the QRPA of Ref. [7]. Only proton-proton and neutron-neutron pairing are considered. The pairing effective interaction is given by

$$V_\tau(\mathbf{r}, \sigma; \mathbf{r}', \sigma') = V_0^{\tau\tau}\left(1 - \eta\frac{\rho([\mathbf{r} + \mathbf{r}']/2)}{\rho_0}\right)\delta_{\mathbf{r},\mathbf{r}'}[1 - P_{\sigma\sigma'}],$$

where $P_{\sigma\sigma'}$ is the spin exchange operator and where $\rho_0 = 0.16$ fm^{-3} and $\tau = n, p$. Results will be presented below only for the case of surface interaction with parameters given in Table I of Ref. [25]. The selection of nuclei is done starting from a list of 749 even-even nuclei for which the masses have been measured and which have a mass $A \geqslant 8$. In the EV8 code, the single-particle states of the Nilsson Hamiltonian are first obtained to initiate the imaginary-time convergence. For each nuclei, to avoid the convergence towards local minima that sometimes might happen with EV8, we performed four types of Nilsson calculations to initiate the self-consistent convergence: one assuming spherical shape, one oblate, one prolate, and one triaxial deformation. Nuclei are assumed to be spherical if the deformation parameter after the imaginary time verifies $\beta_2 < 0.001$, where the deformation parameter is defined through

$$\beta_2 = \sqrt{\frac{5}{16\pi}}\frac{4\pi}{3R^2 A}\langle\hat{Q}_{20}^{IS}\rangle, \quad (9)$$

with $R = 1.2A^{1/3}$. Altogether, 324 and 263 nuclei have been found to be spherical with SkM* and with Sly4 respectively. The retained nuclei are shown in Fig. 1.

We see that both functionals, even if the region of sphericity is slightly larger for SkM*, are globally in agreement with each other. In particular, in medium and heavy nuclei, spherical nuclei are mainly found around N or Z equal to 50 or 82
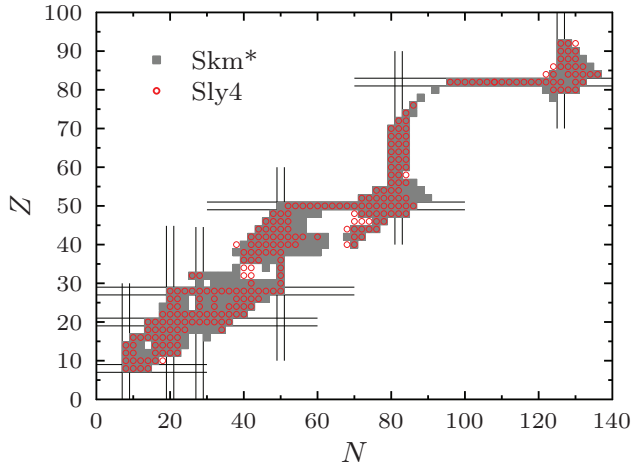
FIG. 1. (Color online) Spherical nuclei retained in the present study using Sly4 (red open circles) and SkM* (grey filled squares). The horizontal and verticals lines indicate protons and neutron magic numbers.

magic numbers. It should be mentioned that, in light nuclei, the spherical shape is mainly preferred due to pairing correlations. Indeed, when pairing is set to zero, many fewer nuclei are found to be spherical in their ground state.

As an additional information, the root-mean-square (rms) radii $\sqrt{\langle r^2 \rangle}$ of different nuclei are shown as a function of the nuclear mass A in Fig. 2. We see that both functionals predict a very similar radius. This is consistent with the fact that their incompressibility moduli are more or less the same: $K_\infty = 216.6$ MeV (SkM*) and $K_\infty = 229.9$ MeV (Sly4). To
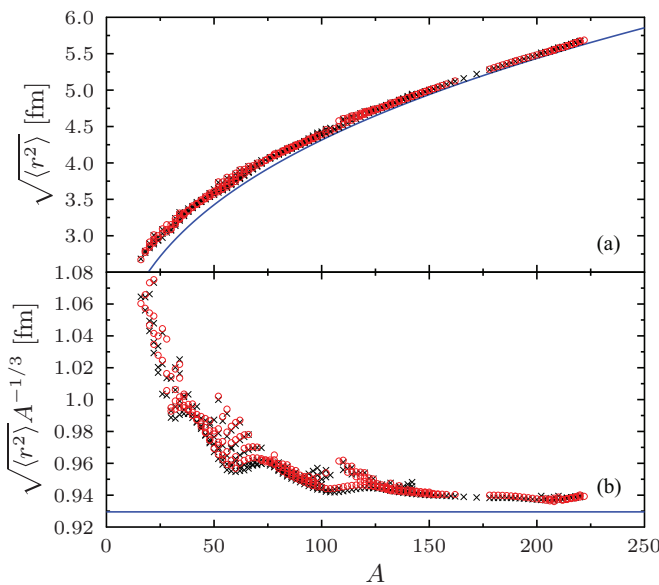

FIG. 2. (Color online) (a) Root-mean-square radius $\sqrt{\langle r^2 \rangle}$ obtained for the selected spherical nuclei using the Sly4 (red circles) or SkM* (black crosses) functional. The simple approximation $\sqrt{\langle r^2 \rangle} = \sqrt{\frac{3}{5}}(1.2A^{1/3})$ is also shown as a reference with a solid blue line. (b) The same quantity divided by $A^{1/3}$.
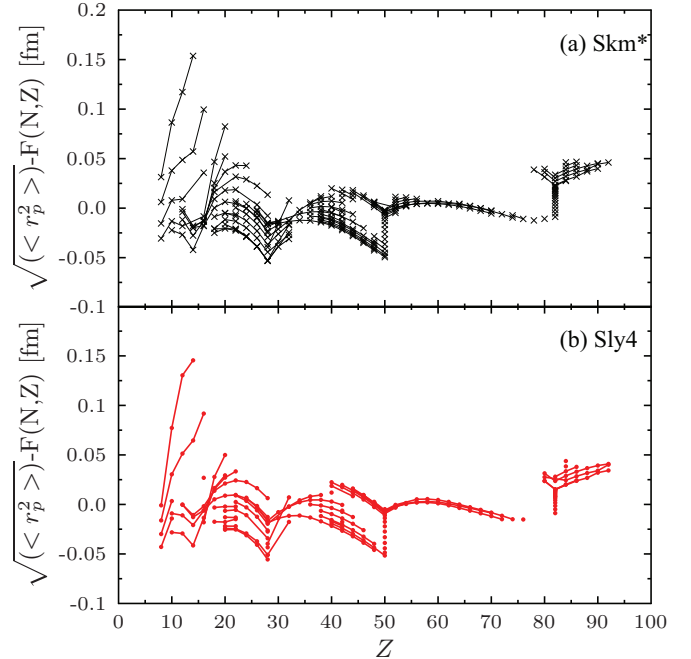

FIG. 3. (Color online) Evolution of the difference between the computed charge rms and the fitted one using formula (10). Results with the Sly4 and SkM* functionals are respectively shown in panels (a) and (b).

further illustrate how shell effects might affect the rms radius, following Ref. [26] we have fitted the calculated proton rms radius using the formula

$$F(N, Z) = \sqrt{\frac{3}{5}} a_0 A^{1/3} \left[1 + \frac{a_S}{A} - a_I \left(\frac{N - Z}{A} \right) \right]. \quad (10)$$

For both functionals, the fit gives $a_0 = 1.22$ fm. For Sly4 $a_S = 2.035$ fm and $a_I = 0.186$ fm, while for SkM* $a_S = 1.9206$ fm and $a_I = 0.189$ fm. Figure 3 displays the difference between the calculated charge rms radius and the fitted value for the Sly4 (b) and SkM* (a) functionals. This figure illustrates the impact of magicity and shell closure that tends to stabilize more compact shapes.

Finally, to characterize the pairing surface interaction, taken from Ref. [25] and used in the present study, the neutron pairing gap obtained for the Ca, Ni, Sn and Pb isotopic chain is displayed as a function of the neutron number in Fig. 4. Several comments can be made. First, these gaps are slightly higher than those reported in Ref. [7]. However, it should be noted that the BCS gap that is a direct output from EV8 is different from the three- (or five-) point gap formula generally used to compare with experiments and that has been also used to adjust the pairing strength in Ref. [25]. We also see in this figure that the present surface pairing interaction leads to nonzero pairing for ^{40}Ca. Finally, we would like to mention that only nuclei that are not too exotic can be studied in the present work due to the well known gas problem appearing in the BCS framework [27]. This is clearly seen in the x axis of Fig. 4 that is much less extended than in Ref. [7]. Nevertheless, the area
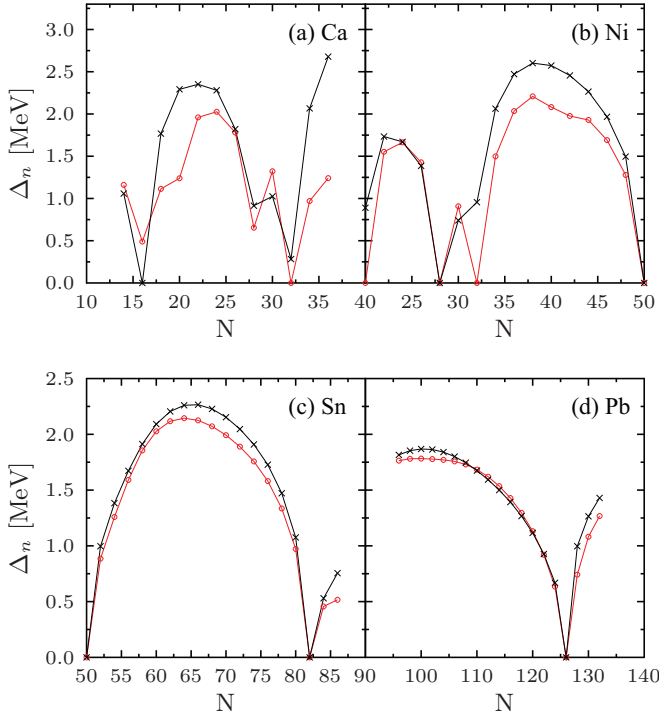
FIG. 4. (Color online) Illustration of the pairing gap in the (a) Ca, (b) Ni, (c) Sn, and (d) Pb isotopes retained in the present work using the Sly4 (red circles) or SkM* (black crosses) functional. Note that the gap is shown even if the nucleus is not spherical.

of the nuclear chart explored in the present work corresponds to nuclei that can be realistically accessed in current and future nuclear reaction experiments.

B. Time-dependent evolution

The time evolution of each nucleus reported in Fig. 1 has been systematically performed using the TDHF3D code [28] with its BCS extension as discussed in Ref. [6]. The initial condition is the spherical ground state obtained with EV8 followed either by a quadrupole isoscalar or isovector boost. The time-dependent evolution is performed in r-space using the mesh-step parameter as in the static case and with a mesh size $L_x = L_y = 2L_z = 22.4$ fm. The numerical time step is given by $\Delta t = 1.5 \times 10^{-24}$ s and the evolutions are followed up a maximal time $T = 50 \times 10^{-22}$ s.

As an illustration of the IS or IV quadrupole evolution, we show in Fig. 5 two illustrations of nuclei: one doubly magic (^{132}Sn) and one with a neutron open shell (^{120}Sn). The corresponding IS and IV response functions are shown in the right side of this figure. These evolutions illustrate the type of behavior typically observed in medium and heavy nuclei. From these figures, one could make the following statements:

(i) *Collective energy:* Both the IS and IV responses present a highly collective state at the expected energies $E \simeq 15$ and 25 MeV respectively.

(ii) *Fragmentation and damping:* The IS GQR displays beating between the high-energy collective modes and the ones at lower energy ($\leqslant 5$ MeV). However the IS motion is not damped for a long time. This stems from the fact that the high-energy peak corresponds to a single highly collective frequency. In contrast, in the IV GQR, an effective damping is observed at short time, stemming from the fragmentation of the strength around the collective energy ($\simeq 25$ MeV) that is similar
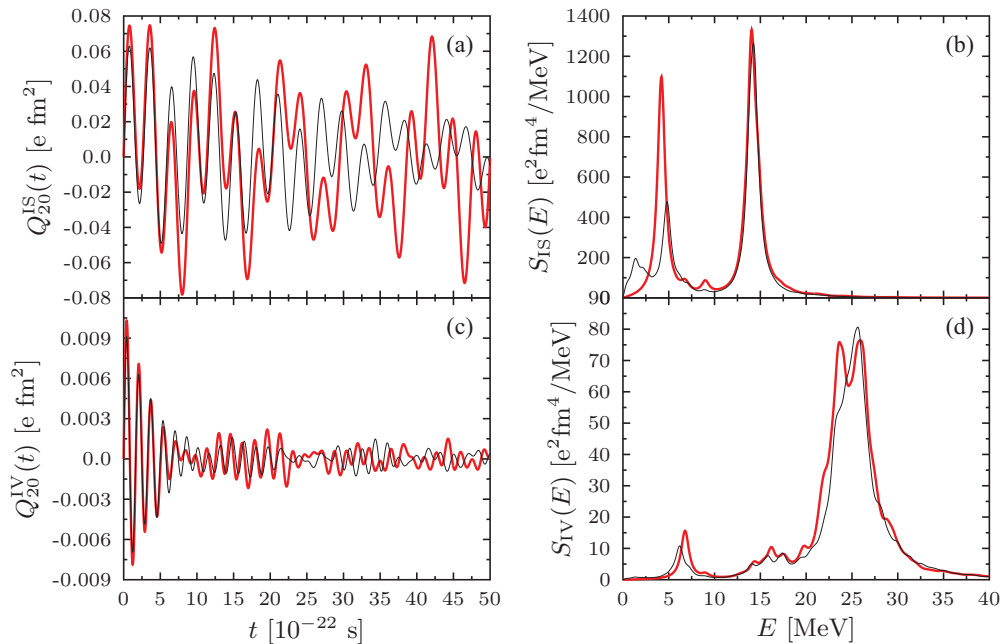

FIG. 5. (Color online) Left: Evolution of the quadrupole moments obtained using TDHF + BCS and the Sly4 functional of the isoscalar (a) and isovector (c) quadrupole moments for a doubly closed shell nucleus ^{132}Sn (red thick solid line) and for a neutron open shell nucleus ^{120}Sn (thin solid line). Right: corresponding response functions using Eq. (6) with a damping factor $\Gamma_0 = 1$ MeV.
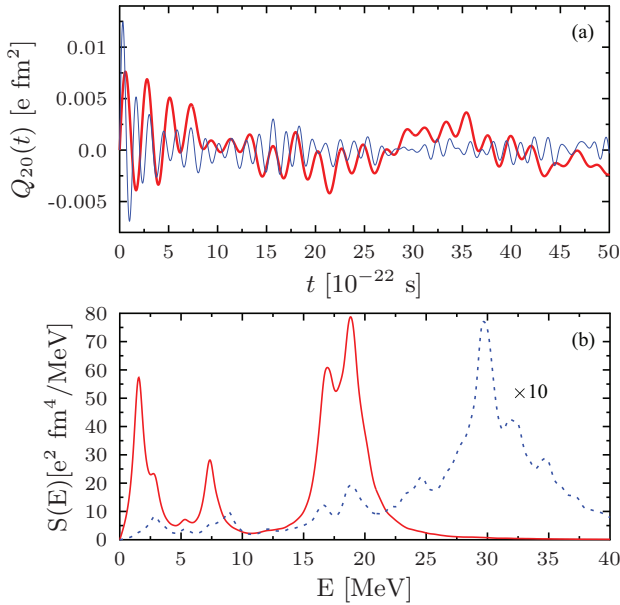
FIG. 6. (Color online) (a) Evolution of the isoscalar (red thick line) and the isovector (blue thin line) quadrupole moments in ^{38}S obtained using TDHF + BCS with the SkM* functional. Note that here the isovector quadrupole moment is multiplied by a factor of 10. (b) Corresponding strength functions for the isoscalar (red thick line) and the isovector (blue dashed line) excitations.

to the Landau fragmentation generally observed in the monopole response of light nuclei.

(iii) *Low-lying state:* Finally, by comparing the two curves in panel (b), we see that the open shell nuclei have an extra low-lying 2^+ state that is expected for superfluid systems (see for instance [7]).

In Fig. 6, a typical evolution and response of a lighter nucleus is shown. For lower-mass systems the fragmentation is enhanced in the IV channel while a small but nonzero fragmentation is seen also in the IS case. We will see below that the fragmentation is seen for $A \leqslant 100$. The different aspects—collective energies, damping, and low-lying states—are discussed systematically below.

III. SYSTEMATIC STUDY OF SPHERICAL NUCLEI

The different aspects discussed in previous section have been systematically investigated. The IS and IV GQR strength distributions computed for all nuclei shown in Fig. 1 can be obtained from the Supplemental Material included with this publication [29].

A. Energy weighted sum rule

The energy weighted sum rule (EWSR) provides a stringent test of the physical and numerical aspects. These sum rules have been extensively discussed in the literature within the energy density functional approaches [30,31] based on Skyrme functional theories and we give below only the constraints that the strength should fulfill.
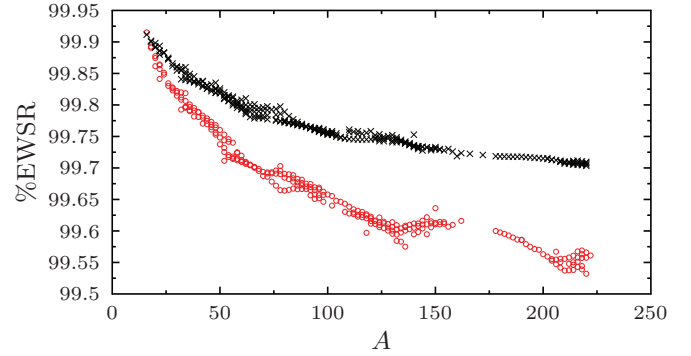

FIG. 7. (Color online) Percentage of the IS GQR EWSR exhausted by the integral of the strength function $S_{IS}(E)$ and obtained with TDHF + BCS code as a function of the mass of the nucleus. The reference sum rule is computed using the right side of Eq. (11). Results obtained with the Sly4 and SkM* functionals are respectively shown using red circles and black crosses.

Starting from the specific excitation operator (4), the EWSR for the IS GQR is given by [32]

$$\int_0^\infty E S_{IS}(E) dE = \frac{e^2 \hbar^2}{8\pi m} \lambda (2\lambda + 1)(A - 1)\langle r^{2\lambda - 2} \rangle$$
$$= 16.501(A - 1)\langle r^2 \rangle \ e^2 \text{fm}^4 \text{MeV}. \quad (11)$$

In the first expression $\lambda = 2$ since we are considering the GQR. The factor $(A - 1)$ instead of A appears due to the center-of-mass correction [33]. The numerical estimates of the sum rule (11) have been made using the value $\hbar = 6.58211 \times 10^{-22}$ MeV s and $m = 1.0446879 \times 10^{-44}$ MeV s^{2}fm^{-2}, while the mean radii $\langle r^2 \rangle$ are those computed directly in the static mean field (Fig. 2). The ratios between the integrals of the strength obtained with TDHF + BCS for different nuclei and the right side of Eq. (11) are shown in Fig. 7. For all nuclei considered here, an error lower than 0.5% is obtained on the total EWSR.

A similar study can be made for the IV GQR. In that case, the sum rule is given by [7,33,34]

$$\int_0^\infty E S_{IV}(E) dE = \frac{e^2 \hbar^2}{8\pi m} \frac{(1 - A)}{A} \lambda (2\lambda + 1)$$
$$\times \left(\frac{N^2 Z}{A^2} \langle r^{2\lambda - 2} \rangle_p + \frac{N Z^2}{A^2} \langle r^{2\lambda - 2} \rangle_n \right)$$
$$+ C_{IV}(\lambda), \quad (12)$$

For $\lambda = 2$, $\langle r^{2\lambda - 2} \rangle_{p/n}$ identifies with the proton and neutron mean radii that are again estimated directly with EV8. C_{IV} is the standard corrective term that stems from the momentum part of the Skyrme functional. For the IV GQR, we have [7]

$$C_{IV}(\lambda = 2) = \frac{e^2}{4} \left\{ t_1 \left(1 + \frac{x_1}{2} \right) + t_2 \left(1 + \frac{x_2}{2} \right) \right\}$$
$$\times \int |\nabla[r^2 Y_{20}(\Omega)]|^2 \rho_n(\mathbf{r}) \rho_p(\mathbf{r}) d\mathbf{r}, \quad (13)$$

where ρ_p and ρ_n are the neutron and proton local densities. The percentage of the EWSR exhausted by the IV strength and obtained with TDHF + BCS are systematically shown in
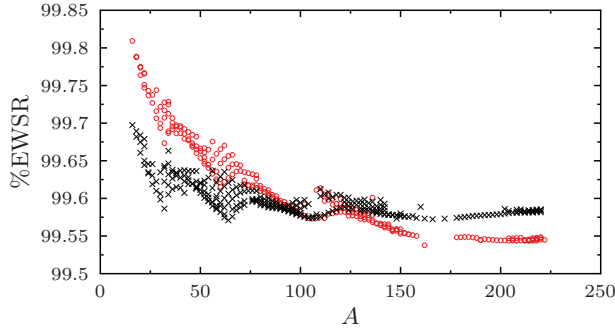
FIG. 8. (Color online) The same as Fig. 7 for the IV GQR.

Fig. 8. Again, almost 100% of the strength is exhausted. It can be noted that the residual error on the EWSR increases as the mass increases. This error is mainly due to the mesh step. For instance, decreasing the mesh step from 0.8 to 0.6 fm in ^{128}Sn for the SkM* case reduces the error from 0.28% to 0.08% for the IS GQR and from 0.41% to 0.10% for the IV GQR.

B. GQR: Mean energy and width

For each nucleus, the mean collective energy and width of the high-lying giant resonance has been extracted by fitting the main collective peak with a Lorentzian distribution,

$$L(E) = \frac{a_0 \Gamma_C}{2\pi} \frac{1}{(E - E_C)^2 + (\Gamma_C/2)^2}, \qquad (14)$$

where a_0, E_C, and Γ_C are the fitting parameters. While E_C is rather insensitive to the damping factor Γ_0, Γ_C mixes physical effects associated with the strength fragmentation (associated with a physical width Γ) with the assumed smoothing parameter Γ_0. By changing the value of Γ_0, it can be shown that the physical width can be simply obtained through the linear relation

$$\Gamma \simeq \Gamma_C - \Gamma_0. \qquad (15)$$

The above strategy to obtain the mean energies and widths is much more precise than the method based on weighted moments of the strength, i.e.,

$$E_C \simeq \frac{m_1}{m_0}, \quad \Gamma_C \simeq \sqrt{m_2/m_0 - (m_1/m_0)^2}, \qquad (16)$$

where m_k stands for the moment of order k of the strength in a restricted region of energy. We have found that this method is too sensitive to the integration region as well as to the smoothing parameter Γ_0.

The collective energy, denoted as E_{2+}, and the width Γ obtained after the fit in combination with Eq. (15) are systematically reported as a function of the mass of the nucleus in Fig. 9. Some experimental data taken from [8] are also shown as a reference.

Focusing first on the mean collective energy, we see that both functionals provide the correct order of magnitude of the energy over the nuclear chart with the proper A dependence. The SkM* functional is systematically closer to experimental observation. However, one should keep in mind that such a direct comparison should be made with care due to the fact that the technique used to get the collective energies and widths
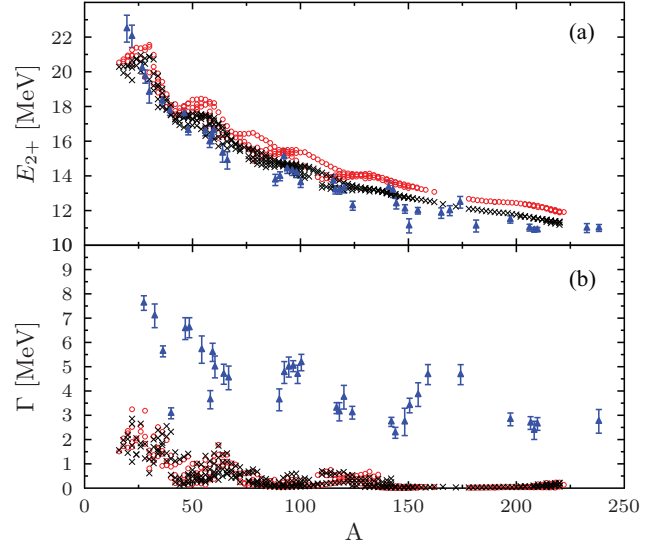

FIG. 9. (Color online) Collective energy (a) and width (b) of the IS GQR systematically obtained for spherical nuclei using the SkM* (black crosses) and Sly4 (red circles) functionals. The blue triangles correspond to experimental data taken from [8].

as well as the energy range considered experimentally might differ from the ones we used.

Interestingly enough, the Sly4 functional gives collective energies that are systematically higher compared to the SkM* case by almost 1 MeV for $A \geqslant 70$. Such a sensitivity in IS GQR has been already pointed out in Refs. [35,36]. It should be noted that a 1 MeV difference, in view of desired accuracy for EDF, is significant enough that the GQR might become a global criteria for the validity of a given functional parametrization.

Panel (b) of Fig. 9 illustrates that the present mean-field calculation completely misses the fragmentation of the strength. The strength function is slightly fragmented for light nuclei but for medium and heavy nuclei ($A > 70$) the high-lying collective energy essentially corresponds to a single collective energy without any spreading. This is clearly at variance with the experimental observation where a rather significant fragmentation is systematically observed. This discrepancy is not surprising since a mean-field theory is expected to reproduce one-body observables but cannot really include two-body effects. In the case of giant resonances, the fragmentation of the strength reflects the coupling to complex internal degrees of freedom such as the coupling to two particles and two holes induced by in-medium collisions [37] or the coupling to low-lying surface modes [38,39]. See for instance the extensive discussion in Ref. [40]. As we know from QRPA calculation, the inclusion of pairing correlations does not cure this problem.

To complete the study, the collective energy and width of the IV GQR are also shown in Fig. 10. The collective energies of both functionals are in global agreement with the experiments except for light nuclei. Regarding the width, the situation is slightly different compared to the IS case since the collective response is always fragmented. The fragmentation obtained with the mean-field theory accounts approximately for half of the fragmentation observed experimentally.
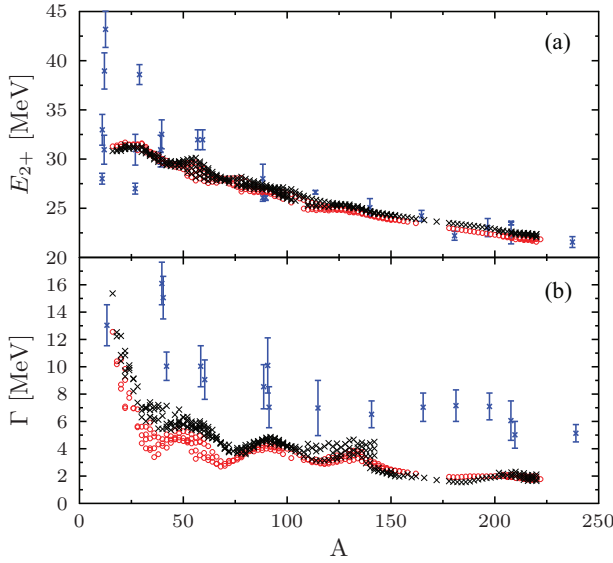
FIG. 10. (Color online) The same as Fig. 9 for the IV GQR. The experimental data are taken from [16,41].

It is interesting to note that the repartition of the EWSR between the low- and high-energy sectors in the IV case is completely opposite compared to the IS GQR. The non-negligible fraction of the EWSR observed at low energy for light nuclei $A \leqslant 50$ vanishes for larger mass, leading to almost 100% of the strength at high energy in heavy nuclei.

C. Average behavior

The IS and IV GQR energies can be appropriately fitted using a polynomial expansion in powers of $A^{-1/3}$, i.e.,

$$\overline{E_{2^+}}(A) = a_1 A^{-1/3} + a_2 A^{-2/3} + a_3 A^{-1} + \cdots . \quad (17)$$

Truncating at second order provides a rather good description of the IS GQR but fails to reproduce the IV GQR. In all cases, a polynomial of order 3 gives an excellent fit of the average energy evolution along the nuclear chart. In Table I, the set of a_i parameters obtained for the IS and IV energies and for the two considered forces is reported. Results of the fit are shown in Fig. 11 where the quantity $A^{1/3} E_{2^+}(A)$ is displayed as a function of the mass A for the two Skyrme functionals. For the sake of completeness we also give in Table I the coefficients obtained by fitting the experimental points displayed respectively in Figs. 9 and 10 using expression (17).

TABLE I. Parameters deduced for the fit of the IS and IV main collective energies with a third-order polynomial in $A^{-1/3}$, Eq. (17).

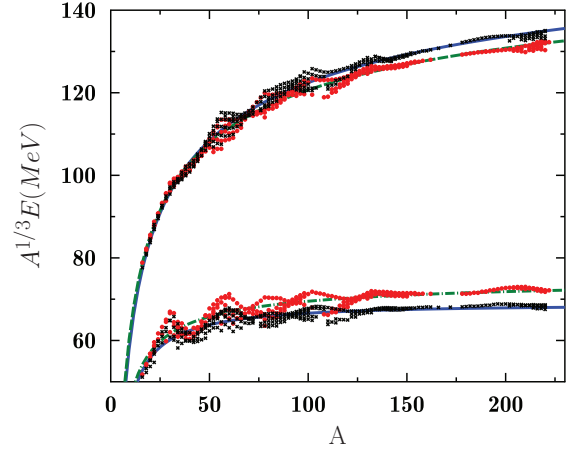|	a_1 (MeV)	a_2 (MeV)	a_3 (MeV)
IS SkM*	65.03	52.93	−211.67
IS Sly4	75.50	3.13	−143.69
IS expt.	72.61	−37.45	0.002
IV SkM*	177	−255.383	10.05
IV Sly4	169.36	−223.16	−13.06
IV expt.	165.19	−182.09	−37.24

FIG. 11. (Color online) Evolution of the quantity $A^{1/3} E_{2^+}(A)$ as a function of mass. The IS (lowest energy) and IV (highest energy) energies are reported for the SkM* and Sly4 functional using respectively black crosses and red filled circles. Result of the fit using a third-order polynomial with parameters reported in Table I are shown with blue solid and green dot-dashed lines for the SkM* and Sly4 functionals respectively.

D. Shell effect on the GQR response

Shell effects are expected to induce small oscillations around the average dependence of the GQR energies as a function of mass. Thanks to the previous analysis, the local fluctuations of the mean energy can be deconvoluted from the average by considering the quantity

$$\Delta E(A) = E_{2^+}(A) - \overline{E_{2^+}}(A), \quad (18)$$

where $E_{2^+}(A)$ is the collective energy while $\overline{E_{2^+}}(A)$ is computed from formula (17). This quantity is systematically reported as a function of the neutron number N in Fig. 12 for the IS and IV GQRs. Similar curves (not shown) are obtained when ΔE is plotted as a function of the proton number Z.

As expected, we do observe several maxima that exactly match the locations of shell closure at magic numbers ($N = 28, 50,$ and 82). This is due to the appearance of larger gaps in single-particle effective energies inducing larger energies of particle-hole excitations from which the collective states are built up. Interestingly enough the deviation ΔE also presents some minima that turn out to be exactly located at the positions of the harmonic oscillator magic numbers without spin-orbit effect ($N = 20, 40,$ and 70). As we will see below, this effect could be understood as a competition between the conserved parity during the excitation and the pairing correlations.

IV. PAIRING EFFECT ON THE GQR RESPONSE

In Ref. [6] it was shown that one of the main effects of pairing on dynamics is to induce partial occupation numbers of single-particle orbitals. This effect can already be accounted for at the mean-field level without pairing by considering a statistical ensemble of independent particles instead of a Slater determinant. In this case, considering an open shell nucleus, the occupation numbers of the last occupied shell are no longer
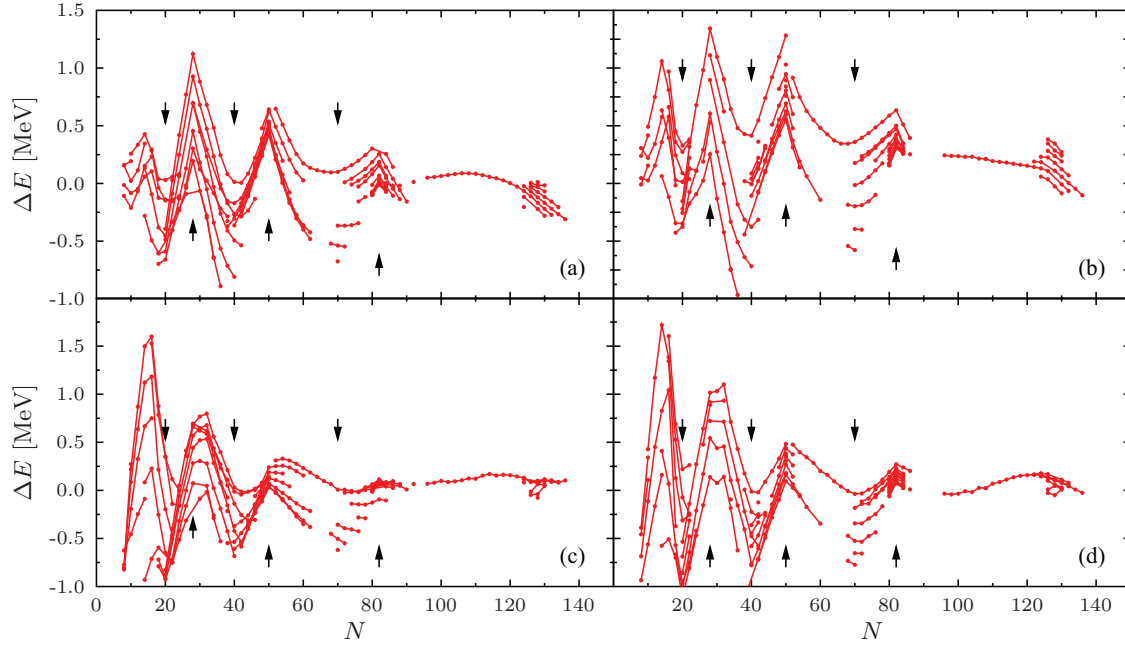
FIG. 12. (Color online) Local fluctuations ΔE of the IS GQR [panels (c) and (d)] and the IV GQR [panels (a) and (b)] as a function of the neutron number N using Sly4 [panels (b) and (d)] and SkM* [panels (a) and (c)]. The up arrows indicate the magic numbers (including spin-orbit effect) ($N = 28, 50, 82$) while the down arrows correspond to the original harmonic oscillator magic numbers without the spin-orbit effect ($N = 20, 40, 70$).

zero or one but are equal to the number of nucleons in the shell divided by the shell degeneracy; this is the so-called equal-filling approximation. For the reason discussed in Ref. [6], this approximation can be regarded as the no-pairing reference for TDHF + BCS.

In Figs. 13 and 14, the IS GQR and IV GQR responses are displayed using different approximations for the evolution. Two TDHF + BCS are considered, one where the occupation numbers and correlations are frozen frozen occupation approximation (FOA) in time and one where the full TDHF + BCS equations of motion are solved in time. The FOA has the advantage that it respects the continuity equation, in contrast to TDHF + BCS [5]. Note that since here we consider a single system, this drawback of TDHF + BCS is not crucial.
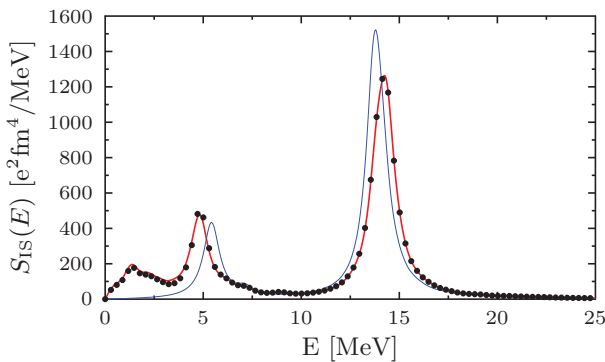
The response functions with pairing are compared with the TDHF + equal-filling approximation case.

The first remarkable aspect is that the two calculations with pairing, i.e., the complete one and the FOA, are exactly on top of each other. This confirms that, in the TDHF + BCS limit, the main effect of pairing on small-amplitude vibrations stems from the initial ground state correlations.

Let us now consider the difference between the TDHF + BCS case and the no-pairing limit. We focus first on the high-energy region ($E \geqslant 10$ MeV). To quantify further the pairing effect on high-lying states, the main peak collective energy of the IS GQR is systematically reported for the Sn isotopes in panel (a) of Fig. 15 and for the three types of evolutions.

Since at shell closure, $N = 50$ and $N = 82$, the HF-BCS ground state identifies with the HF solution, the three theories

FIG. 13. (Color online) Comparison between the IS GQR response obtained with Sly4 using TDHF + BCS (red solid line), TDHF + BCS with FOA (black filled circles), and TDHF (blue thin line) for the ^{120}Sn nucleus.
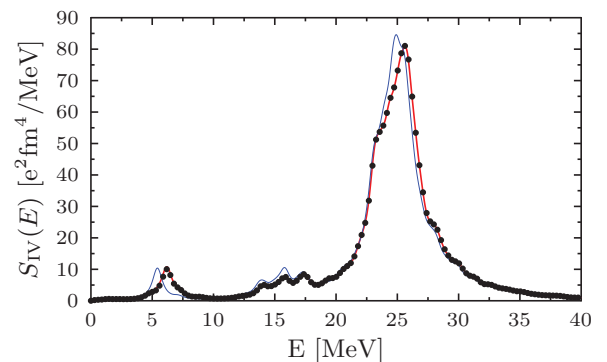

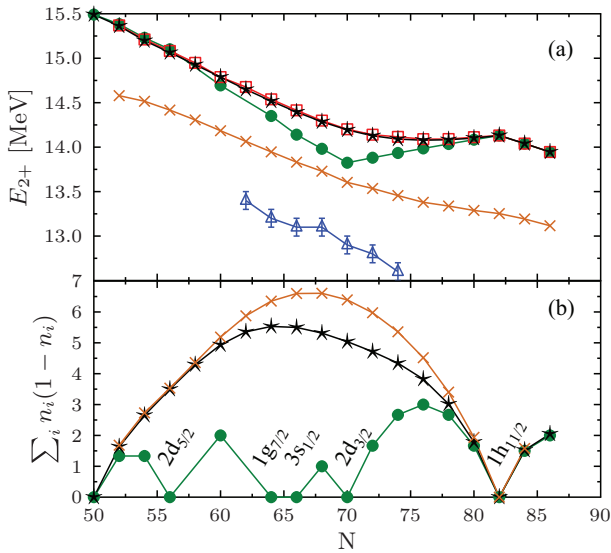FIG. 14. (Color online) The same as Fig. 13 for the IV GQR.

FIG. 15. (Color online) (a) Evolution of the IS GQR energy for the Sn isotopic chain as a function of the neutron number. (b) The quantity $\sum_i n_i(t_0)[1 - n_i(t_0)]$ is shown. This quantity gives a measure of the fragmentation of single-particle occupation numbers around the Fermi energy. Results for TDHF + BCS (red squares), FOA (black stars), and TDHF with the equal-filling approximation (green circles) using the Sly4 functional are shown. The TDHF + BCS results with SkM* (brown crosses) are also shown for comparison. In panel (a), the experimental values from [9] (blue open triangles) are also shown for comparison.

are exactly on top of each other. As N goes from $N = 50$ to $N = 82$, all theories predict a decrease of the GQR energy consistent with the expected $A^{-1/3}$ dependence. However, while the theory with pairing presents a smooth U shape, the TDHF approach is slightly lower and has a minimum at $N = 70$, that corresponds to one of the magic numbers of the harmonic oscillator (HO) without spin-orbit effect. This anomaly observed in the TDHF case is located at the HO shell closure corresponding to the $(1g, 2d, 3s)$ shell, and can be directly assigned to a parity effect. Indeed, the collective excitations have definite parities, here $\pi = +1$. When the number of neutrons increases, the parity of occupied single-particle states changes from positive (below $N = 70$) to negative (above $N = 70$) leading to a sudden change in the particle-hole state on which the collective excitation is built up. The U shape observed in the TDHF + BCS case can be seen as a fossil signature of the parity effect. Indeed, due to pairing correlations, occupation numbers are more fragmented around the Fermi energy. In Fig. 15, the quantity $\sum_i n_i(1 - n_i)$ is shown. This quantity measure the fragmentation of single-particle occupation numbers and falls to zero when all occupation numbers are equal to zero or one. This is the case in the BCS approximation at (spin-orbit) magic number or in the TDHF case when a subshell is fully occupied. Again, except around magic numbers, the fragmentation is more pronounced in the BCS compared to the TDHF case. In particular, around $N = 70$, single-particle states are partially occupied in BCS. Accordingly, the anomaly observed in TDHF is reduced but still yields the U shape. For the SkM* functional

the U shape is less pronounced because the fragmentation is larger than with Sly4. As seen in Fig. 12, the U shape that results from the competition between parity conservation and paring is observed all along the mass table (down arrows) but tends to be less pronounced as the mass increases.

In any case, we see that the difference between the cases with or without pairing is less than the difference observed using different functionals (Sly4 and SkM* here). Our conclusion is that the main source of uncertainty in the prediction of high-lying GQR collective states stems from the functional used in the mean-field channel. We also see that all approximations lie above the experimental values. This might appear as a failure of the theory. However, one should keep in mind that correlations beyond the present approach that account for instance for ph-phonon coupling are expected to shift, most likely down the collective frequencies [40].

1. Systematic of low-lying 2+ mode

Pairing is known to play a crucial role in the low-lying 2^+ states (see for instance the discussion in Ref. [42]) at least due to the induced fragmentation of the single-particle occupation numbers near the Fermi energy. While the high-energy sectors of the response are only slightly dependent on the treatment of (i) pairing effects and (ii) dynamical reorganization of single-particle occupation numbers, the situation is completely different in the low-energy part. Figure 13 illustrates that calculations without pairing (TDHF with equal filling) present a single peak at low energy around $E \simeq 6$ MeV; the full TDHF + BCS and the FOA dynamics display a more fragmented strength at low energy. In particular, new peaks are present at very low energy.

In order to have the first 2^+ energy and the corresponding transition probability, we used a different excitation operator that acts only on protons,

$$\hat{Q} = e \sum_{i=1}^{Z} r_i^2 Y_{20}(\Omega_i). \tag{19}$$

The energy of the lowest peak obtained with TDHF + BCS has been systematically obtained by fitting the strength using the formula (A2) for energies $E \leqslant 7$ MeV (see the Appendix). It is worth mentioning that we observed the same difficulty as in Ref. [45] related to the convergence of low-lying states with the model parameters. Even if the nucleus have very low β_2 values, there is a slight dependence of the response on the nucleus orientation. This dependence is reduced if the mesh parameter decreases and is not seen in the FOA limit. To reduce this effect, we have selected only nuclei which have $\beta_2 < 10^{-8}$. This leads to an ensemble of 112 nuclei.

The results are reported as a function of mass in panel (a) of Fig. 16; for comparison, the results of QRPA and the experimental values of the first 2^+ are also shown. In order to quantify the agreement between the TDHF + BCS and QRPA theories, the standard deviation

$$\sigma = \sqrt{\frac{1}{N} \sum_i^N \left(E_i^{\text{calc}} - E_i^{\text{exp}} \right)^2} \tag{20}$$
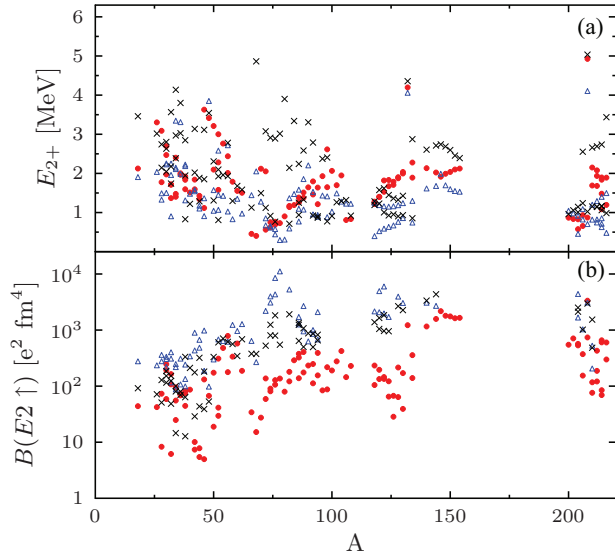
FIG. 16. (Color online) Systematic comparison between the lowest 2^+ energy (a) and transition probability (b) obtained with TDHF + BCS using the Sly4 functional (red filled circles) and the experimental first 2^+ excited state (blue open triangles) from [43]. The QRPA results from [7,44] are also shown for comparison (black crosses).

was computed. For the TDHF + BCS theory $\sigma = 0.77$ MeV, while for QRPA from [44] $\sigma = 1.00$ MeV for the same set of nuclei. Note that the effective interactions used in the pairing channel are different in the two models. The small deviation shows that TDHF + BCS, while being less general than the full TDHFB approach can be rather accurate.

The situation is much less satisfactory for the $B(E2,\uparrow)$ values. Once the lowest peak has been fitted using Eq. (14) and assuming that the physical width is zero for this peak, i.e., $\Gamma_C \simeq \Gamma_0$, then the fitted parameter a_0 identifies with the transition probability $|\langle\Psi_0|\hat{Q}|\Psi_1\rangle|^2$. The $B(E2,\uparrow)$ value is computed through [22]

$$B(E2,\uparrow) = (2\lambda + 1)|\langle\Psi_1|\hat{Q}|\Psi_0\rangle|^2, \qquad (21)$$

with $\lambda = 2$ for a quadrupole excitation. The transition probabilities obtained in this way are systematically reported in panel (b) of Fig. 16. It was already noted in Ref. [44] that the QRPA leads to a significant underestimation of $B(E2,\uparrow)$ compared to experiments. The situation is even worse in the present TDHF + BCS calculation where the computed $B(E2,\uparrow)$ is always lower compared to the QRPA case, sometimes by an order of magnitude. We have investigated how a change of the pairing strength, pairing interaction type (constant pairing, volume, etc.), or particle number conservation through projection on a good particle might affect the response. While the high-energy sector is rather insensitive to any of these effects, the low-energy part is generally found to vary. However, at maximum a factor of 2 of increase or decrease is obtained that could not cure the underestimation problem. Our conclusion is that the TDHF + BCS approach is predictive for the energies of the low-lying state but not for $B(E2,\uparrow)$. It seems that the QRPA, and thus TDHFB, improve the comparison but still miss part of the collectivity.

V. EXTRACTION OF THE DENSITY DEPENDENCE OF THE SYMMETRY ENERGY FROM THE IS AND IV GQR

The possibility to measure more precisely the IV GQR in nuclei [16,17] was recently proposed as a possible way to access to the symmetry energy at density lower than the saturation density [19]. In Ref. [19], a precise analysis was made on the specific ^{208}Pb nucleus. The aim of our work is certainly not to give a detailed discussion of the symmetry energy. However, we illustrate below how a systematic study made on a large scale can bring additional information.

In the present work, we follow closely Ref. [19]. In that work, it was shown that an approximation of the symmetry energy S is given by the formula

$$S(A) \simeq \frac{\varepsilon_F^\infty}{3}\left\{\frac{A^{2/3}}{8(\varepsilon_F^\infty)^2}\left[\left(E_{2^+}^{IV}\right)^2 - 2\left(E_{2^+}^{IS}\right)^2\right] + 1\right\}, \qquad (22)$$

where ε_F^∞ is the infinite nuclear matter Fermi energy at saturation, that is assumed here to be equal to 37 MeV. $E_{2^+}^{IS}$ and $E_{2^+}^{IV}$ are respectively the isoscalar and isovector collective energies.

The quantity $S(A)$ is displayed in Fig. 17 using the IS and IV GQR main peak energies reported in panel (a) of Figs. 9 and 10. Following Ref. [46], the mass dependence
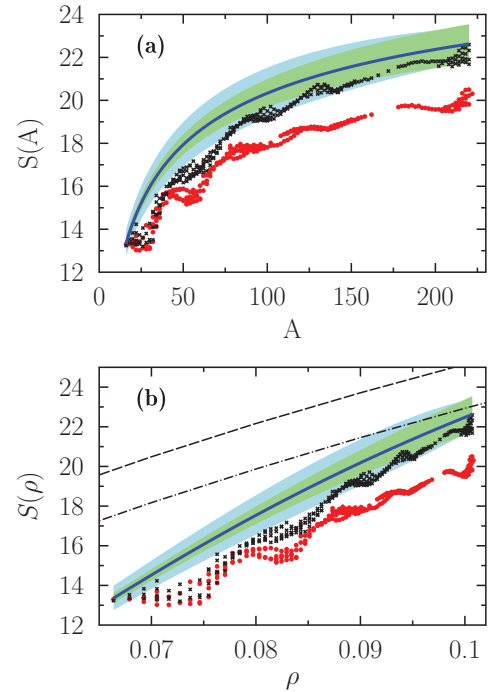

FIG. 17. (Color online) (a) Symmetry energy as a function of the mass A extracted using Eq. (22) for the Sly4 (red filled circles) and the SkM* (black crosses) cases. The blue solid line corresponds to the curve obtained using the experimental data (see text for detail), the light blue area corresponds to the uncertainty when accounting for the error bars on the IV GQR energy solely, while the light green area is the uncertainty when we assume error bars reduced to 500 keV. (b) The same as in panel (a) except that the symmetry energy is displayed as a function of the density. The symmetry energy in infinite nuclear matter (Eq. (4) of Ref. [47]) is also shown for the Sly4 (dashed line) and SkM* (dot-dashed line) cases.

can be transformed into an effective density dependence using

$$\rho = \rho_0 - \rho_0/(1 + cA^{1/3}), \tag{23}$$

where c is set to impose $\rho = 0.1$ fm^{-3} for ^{208}Pb. Here ρ_0 stands for the saturation density that corresponds to $\rho_0 = 0.16$ fm^{-3} for both functionals [23,24], leading to $c = 0.28$. In panel (b) of Fig. 17, the quantity S obtained with Eq. (22) is shown as a function of the density ρ deduced from the formula (23).

Although the IV GQR data are rather poor, similar curves can be obtained using the experimental points reported in Figs. 9 and Fig. 10. To smooth out the uncertainty on experimental collective energies and be able to get information on a wider range of nuclei, we have used the polynomial fit of the experimental points, Eq. (17), instead of the experimental points themselves. Using parameters reported in Table I, a mean tendency of the IS and IV GQRs can be computed for all masses that can be used in formula (22). The results is shown by the solid line in Fig. 17. The error bars, especially on the IV GQR are rather large (1–2 MeV). To see the effect of the IV GQR, we also show in Fig. 17 with the light blue area the uncertainty due to such error bars. The lower and upper boundaries of the area are obtained by using the IV collective energy plus or minus the energy error bars (where the experimental error bars have been fitted by a simple linear function). Finally, we also show in the figure the density dependence of the symmetry energy obtained with the Skyrme functional in infinite nuclear matter, called hereafter S_∞, whose expression can be found for instance in Refs. [47,48].

With all these curves at hand some interesting conclusions can be drawn. First, comparing the results obtained with the two Skyrme functionals, we see that for low masses, $A \leqslant 70$, both functionals agree with each other. However, as the mass increases, a significant difference can be observed in the symmetry energy extracted with (22). This difference can obviously be traced back to the difference observed in the collective peak energies. It should be noted that the symmetry energy is calculated as a difference of energies of collective peaks. Such differences might still lead to the same value for $S(\rho)$. However, we see that the IS peak in SkM* is systematically lower compared to Sly4 while for the IV peak it is the opposite. Therefore, the differences in energies add up and cooperate to further show up in the finite system symmetry energy.

The symmetry energies extracted from the GQR are systematically lower than the ones obtained analytically in infinite nuclear matter. In particular, analytical expressions lead to higher symmetry energies in Sly4 (dashed line) compared to SkM* (dot-dashed line) while the opposite is seen from the GQR based symmetry energy. It could also be noted that a rather significant difference is observed between $S_\infty(\rho)$ and the GQR based symmetry energy. Besides the absolute value, the slope is also different between the infinite system and finite system cases. These differences clearly point out subtle finite size effects when Eq. (22) is used, deserving more studies that are out of the scope of the present work.

Applying formula (22) with experimental collective energies already gives gross properties of the symmetry energy as a function of mass. The main source of uncertainty is coming from the very few measurements made for the IV GQR and from their large error bars. Nevertheless we see that the experimentally deduced symmetry energy is globally in agreement with the SkM* prediction for density above 0.085 that corresponds to $A \geqslant 70$, while it is not with the Sly4 case. To illustrate the impact of improving the measurement precision, we have artificially reduced the error bars down to 500 keV (light green filled area).

VI. CONCLUSION

The IS and IV responses in spherical nuclei have been obtained over a large set of nuclei using the TDHF + BCS approach based on different Skyrme energy density functionals. The present study is first a proof of principle that such an approach is fast and simple enough to make possible qualitative and quantitative systematics over the nuclear chart. It is shown that the time-dependent EDF method globally reproduces the average evolution of the main collective energy but, due to the missing two-body effects, cannot reproduce its spreading width. A careful analysis has shown that the mean collective energy does depend rather significantly on the Skyrme functional. The dependence is large enough to eventually use the GQR as a criteria of selection of the functional itself. In the present work, it is shown that the SkM* reproduces much better the experimental IS GQR than the Sly4 functional.

Besides the global effects, the local fluctuations due to shell structure effects, the parity conservation, as well pairing are discussed. It is shown that all these effects might contributes locally to the fluctuations around the average properties. While around magic numbers the shell stabilization induces an increase of the GQR energy, in between magic numbers the GQR presents a U shape that is the result of the competition between pairing and parity effects.

The possibility to describe low-lying 2^+ state with our time-dependent approach is discussed. It is shown that the TDHF + BCS method is able to globally describe the energy of the first 2^+ state but strongly underestimates the transition operator.

Finally, the possible extraction of the density dependence of the symmetry energy from IS and IV GQRs is discussed. We show that a large-scale calculation like the one presented here can provide interesting information on the symmetry energy but requires a better understanding of finite-size effects and would benefit from high-precision measurement of the IV GQR.

All response functions used in the present work can be downloaded with the Supplemental Material [29].

APPENDIX: STRENGTH FUNCTION OBTAINED IN REAL TIME CALCULATIONS

In order to determine the peak with the lowest energy, we have developed a fitting procedure that take into account

the finite time of the evolution. Starting from the evolution of $Q(t)$,

$$Q(t) \simeq Q(0) + i\lambda \sum_\nu |\langle \Psi_\nu | \hat{Q} | \Psi_0 \rangle|^2 \left(e^{-i\frac{E_\nu t}{\hbar}} - e^{i\frac{E_\nu t}{\hbar}} \right), \tag{A1}$$

the Fourier transform, obtained with an integration between the time t_0 and the final time T, with a damping factor Γ_C, becomes

$$S_Q(\omega) = -\frac{1}{\pi \lambda \hbar} \mathrm{Im} \int_0^T e^{-\frac{\Gamma_C}{2\hbar}t} [Q(t) - Q(0)] \sin(\omega t) dt$$

$$= \frac{1}{\pi} \sum_\nu^N |\langle \Psi_\nu | \hat{Q} | \Psi_0 \rangle|^2 \left\{ \frac{-\frac{\Gamma_C}{2}\left[e^{-\frac{\Gamma_C T}{2\hbar}} \cos\left(\frac{(E-E_\nu)T}{\hbar} \right) - 1 \right] + (E - E_\nu) e^{-\frac{\Gamma_C T}{2\hbar}} \sin\left(\frac{(E-E_\nu)T}{\hbar} \right)}{(\frac{\Gamma_C}{2})^2 + (E - E_\nu)^2} \right.$$

$$\left. - \frac{-\frac{\Gamma_C}{2}\left[e^{-\frac{\Gamma_C T}{2\hbar}} \cos\left(\frac{(E+E_\nu)T}{2\hbar} \right) - 1 \right] + (E + E_\nu) e^{-\frac{\Gamma_C T}{2\hbar}} \sin\left(\frac{(E+E_\nu)T}{\hbar} \right)}{\left(\frac{\Gamma_C}{2} \right)^2 + (E + E_\nu)^2} \right\}. \tag{A2}$$

In the present article, fits are performed using the above formula that accounts for both the smoothing parameter and the finite time interval for the evolution. In practice, for the low-lying state, due to the possible appearance of several peaks, the fit is made assuming up to $N = 7$ peaks in the energy region $E \leqslant 7$ MeV.

[1] Y. Hashimoto, Eur. Phys. J. A **48**, 1 (2012).

[2] B. Avez, C. Simenel, and Ph. Chomaz, Phys. Rev. C **78**, 044318 (2008).

[3] I. Stetcu, A. Bulgac, P. Magierski, and K. J. Roche, Phys. Rev. C **84**, 051309(R) (2011).

[4] S. Ebata, T. Nakatsukasa, T. Inakura, K. Yoshida, Y. Hashimoto, and K. Yabana, Phys. Rev. C **82**, 034306 (2010).

[5] G. Scamps, D. Lacroix, G. F. Bertsch, and K. Washiyama, Phys. Rev. C **85**, 034328 (2012).

[6] G. Scamps and D. Lacroix, Phys. Rev. C **87**, 014605 (2013).

[7] J. Terasaki and J. Engel, Phys. Rev. C **74**, 044301 (2006).

[8] F. E. Bertrand, Nucl. Phys. A **354**, 129c (1981).

[9] T. Li *et al*., Phys. Rev. C **81**, 034309 (2010).

[10] Y.-W. Lui, D. H. Youngblood, S. Shlomo, X. Chen, Y. Tokimoto, Krishichayan, M. Anders, and J. Button, Phys. Rev. C **83**, 044327 (2011).

[11] M. Buenerd, J. Phys. (Paris) Colloq. **45**, C4-115 (1984).

[12] D. H. Youngblood, P. Bogucki, J. D. Bronson, U. Garg, Y.-W. Lui, and C. M. Rozsa, Phys. Rev. C **23**, 1997 (1981).

[13] W. T. A. Borghols *et al*., Nucl. Phys. A **504**, 231 (1989).

[14] M. M. Sharma, W. T. A. Borghols, S. Brandenburg, S. Crona, A. van der Woude, and M. N. Harakeh, Phys. Rev. C **38**, 2562 (1988).

[15] S. Brandenburg, Ph.D. thesis, University of Groningen, 1985 (unpublished).

[16] D. A. Sims *et al*., Phys. Rev. C **55**, 1288 (1997).

[17] T. Ichihara, M. Ishihara, H. Ohnuma, T. Niizeki, Y. Satou, H. Okamura, S. Kubono, M. H. Tanaka, and Y. Fuchi, Phys. Rev. Lett. **89**, 142501 (2002).

[18] S. S. Henshaw, M. W. Ahmed, G. Feldman, A. M. Nathan, and H. R. Weller, Phys. Rev. Lett. **107**, 222501 (2011).

[19] X. Roca-Maza, M. Brenna, B. K. Agrawal, P. F. Bortignon, G. Colò, L.-G. Cao, N. Paar, and D. Vretenar, Phys. Rev. C **87**, 034301 (2013).

[20] P. Bonche, H. Flocard, and P.-H. Heenen, Comput. Phys. Commun. **171**, 49 (2005).

[21] C. Simenel, Eur. Phys. J. A **48**, 152 (2012).

[22] P. Ring and P. Schuck, *The Nuclear Many-Body Problem* (Springer-Verlag, Berlin, 1980).

[23] E. Chabanat, P. Bonche, P. Haensel, J. Meyer, and R. Schaeffer, Nucl. Phys. A **635**, 231 (1998).

[24] J. Bartel, P. Quentin, M. Brack, C. Guet and H.-B. Håkansson, Nucl. Phys. A **386**, 79 (1982).

[25] G. F. Bertsch, C. A. Bertulani, W. Nazarewicz, N. Schunck, and M. V. Stoitsov, Phys. Rev. C **79**, 034306 (2009).

[26] B. Nerlo-Pomorska and K. Pomorski, Z. Phys. A **348**, 169 (1994); B. Nerlopomorska and B. Mach, At. Data Nucl. Data Tables **60**, 287 (1995).

[27] J. Dobaczewski, H. Flocard, and J. Treiner, Nucl. Phys. A **422**, 103 (1984).

[28] K.-H. Kim, T. Otsuka, and P. Bonche, J. Phys. G **23**, 1267 (1997).

[29] See Supplemental Material at http://link.aps.org/supplemental/10.1103/PhysRevC.88.044310 for the data file of the IS GQR and IV GQR strength distributions for all considered nuclei in this work.

[30] O. Bohigas, A. M. Lane, and J. Martorell, Phys. Rep. **51**, 267 (1979).

[31] J. P. Blaizot and G. Ripka, *Quantum Theory of Finite Systems* (MIT Press, Cambridge, Massachusetts, 1986).

[32] M. N. Harakeh and A. van der Woude, *Giant Resonances* (Oxford University Press, Oxford, 2001).

[33] G. Colò, L. Cao, N. Van Giai, and L. Capelli, Comp. Phys. Commun. **184**, 142 (2013).

[34] H. Sagawa and G. F. Bertsch, Phys. Lett. B **146**, 138 (1984).

[35] V. O. Nesterenko, W. Kleinig, J. Kvasil, P. Vesely, P.-G. Reinhard, and D. S. Dolci, Phys. Rev. C **74**, 064306 (2006).

[36] V. O. Nesterenko, W. Kleining, J. Kvasil, and P. Vesely, Int. J. Mod. Phys. E **17**, 89 (2008).

[37] D. Gambacurta, M. Grasso, and F. Catara, Phys. Rev. C **81**, 054312 (2010).

[38] D. Gambacurta, M. Grasso, V. De Donno, G. Co, and F. Catara, Phys. Rev. C **86**, 021304 (2012).

[39] M. Brenna, G. Colò, and P. F. Bortignon, Phys. Rev. C **85**, 014305 (2012).

[40] D. Lacroix, S. Ayik, and Ph. Chomaz, Prog. Part. Nucl. Phys. **52**, 497 (2004).

[41] K. Maeda, S. Ito, H. Itoh, O. Konno, H. Matsuyama, T. Murakami, T. Sasaki, T. Suda, M. Takeya and T. Terasawa, J. Phys. Soc. Jpn. **75**, 034201 (2006).

[42] G. F. Bertsch, in *Fifty Years of Nuclear BCS*, edited by R. A. Broglia and V. Zelevinsky (World Scientific, Singapore, 2013), p. 26–39.

[43] S. Raman, C. W. Nestor, Jr., and P. Tikkanen, At Data Nucl. Data Tables **78**, 1 (2001).

[44] J. Terasaki, J. Engel, and G. F. Bertsch, Phys. Rev. C **78**, 044311 (2008).

[45] S. Ebata, Ph.D. thesis, University of Tsukuba, 2011 (unpublished).

[46] M. Centelles, X. Roca-Maza, X. Viñas, and M. Warda, Phys. Rev. Lett. **102**, 122502 (2009).

[47] L.-W. Chen, C. M. Ko, and B.-A. Li, Phys. Rev. C **72**, 064309 (2005).

[48] J. R. Stone, J. C. Miller, R. Koncewicz, P. D. Stevenson, and M. R. Strayer, Phys. Rev. C **68**, 034324 (2003).